Design and Analysis of Dual Stator PMSM With Separately Controlled Dual Three-Phase Winding for eVTOL Propulsion

Sung-Woo Hwang, Dong-Kyun Son, Soo-Hwan Park, Geun-Ho Lee, Young-Doo Yoon, *Senior Member, IEEE*, and Myung-Seop Lim, *Member, IEEE*

***Abstract*— The propulsion system of the electric-powered vertical take-off and landing aircraft requires a high level of performances, including power density, efficiency, noise vibration and harshness, and fault tolerance. Among many types of conventional electric motor, the outer rotor surface-mounted permanent magnet synchronous motor (SPMSM) is widely used for its high power density and low torque pulsation. However, these advantages are degraded when the multiphase winding is applied to secure the fault-tolerance characteristics. To overcome the limit of conventional motor topology, the dual stator permanent magnet synchronous motor with separately controlled dual three-phase winding is proposed. The advantages of the proposed topology are resulted from the feature of mechanical, electrical, and magnetic isolation. To maximize the distinctive feature, a design process considering separated current vector control (SCVC) method is established. A design example is presented to demonstrate the impacts of the proposed design process considering SCVC on the power density maximization, torque harmonic reduction, and efficiency improvement. Finally, the experimental verification is presented to validate the proposed design and control techniques.**

***Index Terms*— Aircraft, design methodology, multiphase winding, permanent magnet synchronous motors (PMSMs).**

I. Introduction

ACCORDING to the trend of electrification for eco-friendly technologies in many fields, the demand for electric propulsion systems for aircraft is increasing [1], [2]. In particular, urban air mobility (UAM), which is expected to solve the various problem related to urban traffic issues, is under development by many automotive companies, startups, and research institutes. Due to its required behaviors, the electric-powered vertical take-off and landing (eVTOL) is mostly adopted by many companies. As the electric motor for the eVTOL propulsion, there are three main requirements. First, high power density and high efficiency are required for longer mileage [3], [4]. Second, the strict noise regulation in the urban area requires the electric motor to exhibit low torque ripple and vibration [5]. Third, the fault-tolerance capability is critical for the aircraft safety [6]. Here, the fault includes the electrical faults such as phase open and shorts.

Among conventional motor topologies, the outer rotor surface-mounted permanent magnet synchronous motor (SPMSM) is mostly used for its advantage of high power density [7]. In addition, its low torque ripple based on the low saliency leads to good NVH quality [8]. To reinforce the fault-tolerance capability, multiphase winding is applied [9], [10]. With the asymmetric six-phase winding, not only the fault-tolerance capability but also the power density can be intensified [11]. However, the magnetic interaction between two winding sets in a single stator affects the motor performance and control stability [9], [12], [13]. Therefore, some advanced control strategies such as vector space decomposition are required [13]. Especially in fault situation, the postfault control strategy considering the coupling effect is important to secure the motor performance [14]–[16]. Therefore, reducing the magnetic coupling between winding sets is required in the electromagnetic design.

Recently, the dual stator structure is increasingly studied due to the advantage despite the complicated manufacturing. This structure is advantageous on the power density due to the structure, which enables high space utilization, and thus, there have been some studies that combine with design techniques for higher torque [17]–[19]. Also, the axial flux motors having multiple stators were studied for high power density [20]. In addition, the configuration consists of two stators and a rotor gives higher degree of freedom (DOF) to determine the motor split ratio that is related to the power density [21]. The high DOF in design of the dual stator structure was utilized to reduce the torque ripple. The slot number combination among two stators is used to reduce the torque ripple [22], and the determination of the angular offset between stator cores can reduce the cogging torque [23]. Since the two stator cores are separated by the rotor in between, the magnetic disturbance between two armatures is much less than the single stator structure, which is advantageous in fault

Manuscript received 1 December 2021; revised 24 February 2022 and 16 May 2022; accepted 3 July 2022. Date of publication 20 July 2022; date of current version 21 October 2022. This work was partly supported by Institute of Information & communications Technology Planning & Evaluation (IITP) grant funded by the Korea government (MSIT) (No. 2020-0-01373, Artificial Intelligence Graduate School Program (Hanyang University)) and the research fund of Hanyang University (202100000670020). *(Corresponding author: Myung-Seop Lim.)*

Sung-Woo Hwang, Soo-Hwan Park, Young-Doo Yoon, and Myung-Seop Lim are with the Department of Automotive Engineering, Hanyang University, Seoul 04763, South Korea (e-mail: supertramph@hanyang.ac.kr; shwanp14@hanyang.ac.kr; yoonyd@hanyang.ac.kr; myungseop@hanyang.ac.kr).

Dong-Kyun Son and Geun-Ho Lee are with the Department of Automotive Engineering, Kookmin University, Seoul 02707, South Korea (e-mail: dkson92@kookmin.ac.kr; motor@kookmin.ac.kr).

Digital Object Identifier 10.1109/TTE.2022.3192353

tolerance [24], [25]. The fault tolerance can be maximized by applying the multiphase winding to the dual stator structure [26]. The high DOF is not only applied to the design but also the current control. By optimizing the current ratio of the outer and inner winding, the loss can be minimized [27]. The aforementioned studies fragmentarily verified various advantages of the dual stator structure; however, comprehensive research on the dual stator structure with multiphase winding is required to figure out the synergy and tradeoff relations between the design and control techniques. In addition, complicated design process and current control strategy caused by the high DOF requires comprehensive investigation.

In this article, a dual stator permanent magnet synchronous motor (PMSM) with separately controlled dual three-phase winding is devised, which optimally utilizes the features based on high DOF in design and control. The contribution of this article is featured by combining the design process and current vector control strategy. In Section II, the novel topology having dual stator with separately controlled dual three-phase is introduced and the fundamental theories, including the *dq*-axis equivalent model, are presented. Subsequently, the expected characteristics of the proposed topology are discussed. In Section III, to alleviate the difficulty in design due to the high DOF system, the simplified design process to achieve high power density is proposed with a practical example. Finally, the experimental verification is included in Section IV.

II. Dual Stator PMSM With Separately Controlled Dual Three-Phase Winding

As the designation implies, this topology is distinguished from conventional motors in mechanical structure and electrical perspectives. From mechanical viewpoint, the proposed topology consists of outer and inner stators, and each stator contains three-phase winding. Since the two winding sets are isolated from each other with a rotor in between, the proposed topology has unique features that can be advantageous, and it requires a complicated design process and an appropriate current vector control method. In this section, the overall features of the proposed topology are introduced, and the detail presented with design example in Section III.

A. Dual Stator Structure

The dual stator structure can be regarded as the integrated structure of the two single stator structures of inner rotor and outer rotor type, as shown in Fig. 1. There are two stators: the outer stator and the inner stator. Both the stators are the same as those of the conventional single stator structure. However, the rotor of the dual stator structure is different from that of the conventional single stator structure. There are two layouts of the permanent magnets (PMs) arrangements: N-N type and N-S type [28]. The N-N type has double-layer arrangement of PMs, and each PM layer interacts with each stator. On the other hand, there is a single-layer arrangement of PMs in the N-S type. The two stators share the single PM layer. The magnetic flux flows radially in the rotor region so that the rotor yoke is not required in the magnetic viewpoint, so that it is advantageous in space utilization. For maximization of the power density, the N-S type was selected in this study.

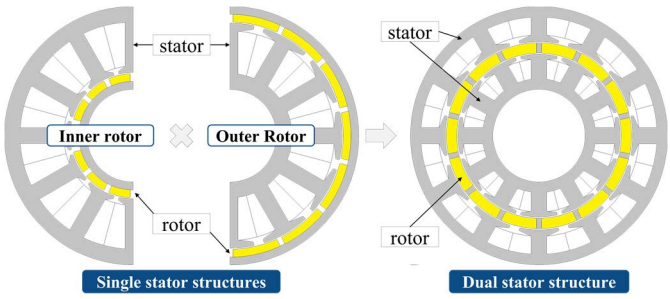

Fig. 1. Mechanical structure of the proposed topology.

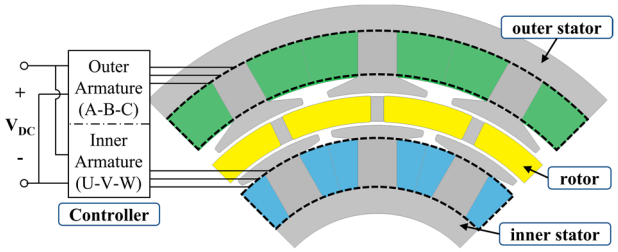

Fig. 2. Electrical system of the proposed topology.

TABLE I
Comparison of Single and Dual Stator Six-Phase Motors

Contents	Single stator	Dual stator
Flux of two winding sets	Overlapped	Separated
Armature MMF	Balanced	Independent
Current phase difference	Fixed (30º or 60º)	Variable
Relative position of stators	N/A	Adjustable

B. Separately Controlled Dual Three-Phase Winding

In the conventional six-phase winding system, including the symmetric and asymmetric topology, the two winding sets are located overlapped by each other in single stator. However, the proposed topology has two of three-phase winding sets placed separately in the two stators, and the two winding sets are controlled individually by the controller, as shown in Fig. 2. Thus, the two winding sets are separated physically and electrically. In addition, these are isolated magnetically also because the magnetic interaction between the two winding sets is much smaller than that of the conventional single stator six-phase system. Due to the magnetic isolation, various distinctive features are available in the proposed topology, as shown in Table I. First, the current amplitudes of the two winding sets can be differently induced since the magnetomotive forces (MMFs) and the outer and inner armatures are not required to be balanced. Furthermore, the current phases can also be controlled differently. In this article, this control method is called separated current vector control (SCVC). Second, this structure has an additional design variable that is the relative position of the two stators. These control and design

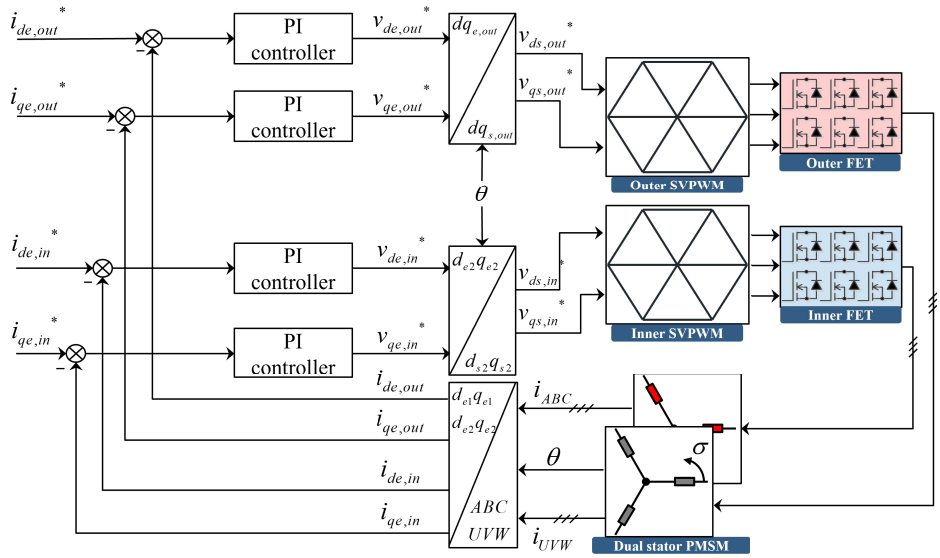

Fig. 3. Block diagram of current control of separately controlled dual three-phase winding.

variables are utilized to optimize the power density and torque pulsation. Unlike the single stator six-phase motors that require complicated space vector decomposition in current control, the double *dq* transformation, which is a simple control algorithm, is applied to control the proposed topology, as shown in Fig. 3.

C. Dq Equivalent Model for SCVC

To design and analyze the proposed topology, the *dq* equivalent model is developed based on the model of the conventional three-phase PMSM. The magnetic circuit consists of three MMF sources: two armatures and a field. Thus, the armature flux linkage can be expressed generally as (1) and transformed to the d- and q-axis as (2)

$$\Psi_{\text{armature}} = \Psi_{\text{self}} + \Psi_{\text{mutual}} + \Psi_{\text{field}} \tag{1}$$

$$\begin{bmatrix} \Psi_{d,\text{out}} \\ \Psi_{q,\text{out}} \\ \Psi_{d,\text{in}} \\ \Psi_{q,\text{in}} \end{bmatrix} = \begin{bmatrix} L_{d,\text{out}} & 0 & M_{d,\text{out}} & 0 \\ 0 & L_{q,\text{out}} & 0 & M_{q,\text{out}} \\ M_{d,\text{in}} & 0 & L_{d,\text{in}} & 0 \\ 0 & M_{q,\text{in}} & 0 & L_{q,\text{in}} \end{bmatrix} \begin{bmatrix} i_{d,\text{out}} \\ i_{q,\text{out}} \\ i_{d,\text{in}} \\ i_{q,\text{in}} \end{bmatrix} + \begin{bmatrix} \Psi_{\text{PM,out}} \\ 0 \\ \Psi_{\text{PM,in}} \\ 0 \end{bmatrix} \tag{2}$$

where Ψ is the flux linkage, L is the self-inductance, M is the mutual inductance between the two armatures, and i is the current. The subscripts d and q are the d- and q-axis components, respectively, and out and in stand for the outer and inner armature, respectively. Ψ_{PM} is flux linkage due to PMs. To be more accurate, the mutual inductance terms are included; however, the terms are much smaller than the self-inductance terms. Based on the magnetic circuit above, the voltage and torque equations are expressed as follows, equations (3) and (4), as shown at the bottom of the next page, where V_o is the induced voltage, T is the torque, and P_n is the number of pole pairs. As can be seen in (3), the induced voltage consists of self-inductance, mutual inductance, and PM components.

D. Fault-Tolerance Characteristics

Generally, multiphase motors, such as the six-phase motor, are used where the superior fault-tolerance property is required [29], [30]. However, the performances of the multiphase motors with single stator are limited in the fault condition, because of the interaction between the healthy and faulted winding sets [12], [14]. In this viewpoint, the proposed topology is advantageous due to the isolation of the winding sets in many perspectives as aforementioned. First, the physical and electrical separation reduces the possibility of the winding fault. Second, even if the fault occurs, the smaller magnetic interaction between two armatures leads to minimized performance degradation compared to the conventional single stator motors. This difference between the two topologies can be demonstrated by comparing the flux path of each armature. The flux paths when only one phase of one winding set is energized (PMs are also not magnetized) are analyzed via finite-element analysis (FEA) with a 14-pole 12-slot example model, which is designed in Section III. Fig. 4(a) shows the winding layouts of the single stator and the dual stator structures. As shown in Fig. 4(b), the flux passes through not only the teeth with the energized winding but also the teeth with other winding set. As shown in Fig. 4(c), on the contrary, the flux generated by each armature flows mostly through the rotor and does not flow through the opposite stator. This implies that the coupling effect between two armature winding sets is much smaller in the case of the dual stator structure. In Fig. 5, the interactions between phases are compared quantitively in terms of the ratio between inductances. Here, L stands for the self-inductance within an armature set and M stands for the mutual inductances in between two armatures. A, B, and C are three phases of outer armature and U, V, and W are three phases of inner armature.

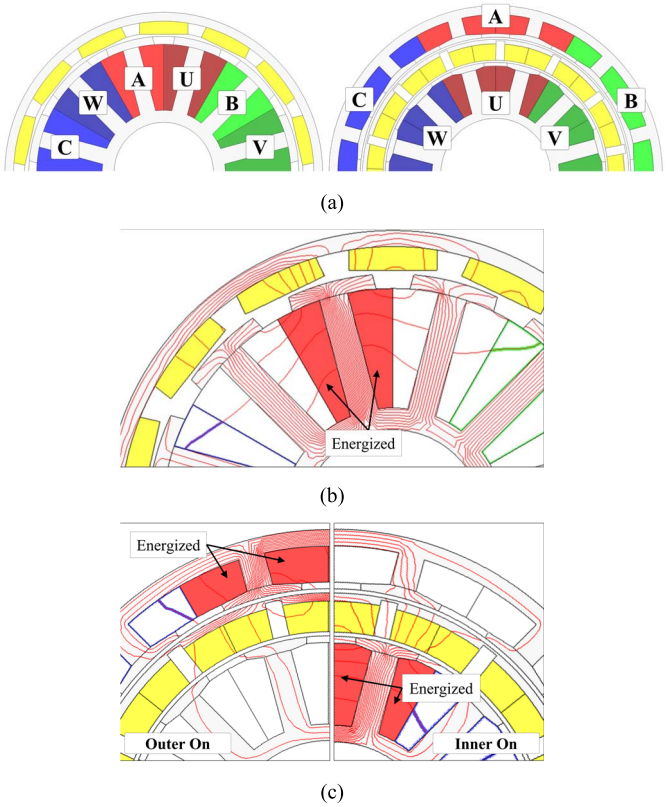

Fig. 4. Magnetic interaction between two armatures. (a) Winding layouts; single stator (left) and dual stator (right). (b) Flux path of single stator structure. (c) Flux path of dual stator structure.

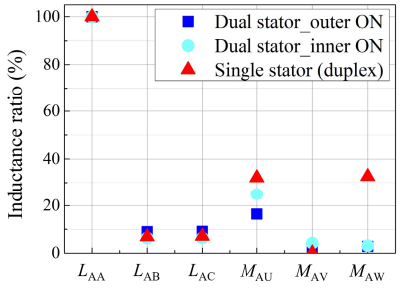

Fig. 5. Inductance ratio comparison.

The inductances are calculated by dividing the flux linkage of an observed phase by the current when only one out of six phases are energized. This method is equally applied to the single and dual stator structures. For example, L_{AA} is obtained by dividing the phase A flux linkage by phase A current, and M_{AW} is obtained by dividing the phase W flux linkage by phase A current. Because the two structures have

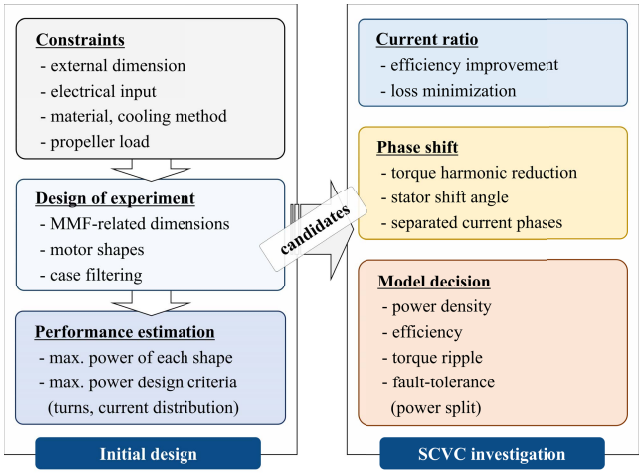

Fig. 6. Design procedure of the proposed topology.

difference level of inductances, they are normalized by L_{AA}. The smaller M_{AU}, M_{AV}, and M_{AW} imply weaker interaction between two winding sets. Therefore, it can be concluded that the six-phase with dual stator structure is advantageous in fault-tolerant characteristics.

III. Design Process Considering Separated Control

The proposed topology aims on securing the requirements of the eVTOL propulsion, including power density, efficiency, torque ripple, and fault tolerance. Since the fault tolerance is granted inherently by the structure, the design process focuses on the other performances. The higher DOF in design and control leads to not only the better performance but also complexity. Accordingly, the power density is maximized separately in the initial design stage, and then, the efficiency improvement and reduction of torque harmonics are dealt with two novel techniques based on the SCVC. The design procedure is shown in Fig. 6. Given the design constraints, numerous shapes are examined with fast and accurate method for maximum power estimation in the initial design stage. Subsequently, few candidates selected and investigated by applying SCVC techniques. Finally, the optimum model is decided.

A. Initial Design for Propeller Load

The split ratio of motor (i.e., outer-diameter-to-air-gap-diameter ratio) is related to the distribution of MMF sources so that it is a key design factor for power density maximization [31]. In the case of dual stator structure, there are two air

$$V_{o,\text{out}} = \omega\sqrt{\left(L_{d,\text{out}}i_{d,\text{out}} + M_{d,\text{out}}i_{d,\text{in}} + \Psi_{\text{PM}}\right)^2 + \left(L_{q,\text{out}}i_{q,\text{out}} + M_{q,\text{out}}i_{q,\text{in}}\right)^2}$$

$$V_{o,\text{in}} = \omega\sqrt{\left(L_{d,\text{in}}i_{d,\text{in}} + M_{d,\text{in}}i_{d,\text{out}} + \Psi_{\text{PM}}\right)^2 + \left(L_{q,\text{in}}i_{q,\text{in}} + M_{q,\text{in}}i_{q,\text{out}}\right)^2} \tag{3}$$

$$T_{\text{out}} = P_n\left\{\Psi_{\text{PM}}i_{q,\text{out}} + \left(L_{d,\text{out}} - L_{q,\text{out}}\right)i_{d,\text{out}}i_{q,\text{out}} + M_{d,\text{out}}i_{d,\text{in}}i_{q,\text{out}} - M_{q,\text{out}}i_{q,\text{in}}i_{d,\text{out}}\right\}$$

$$T_{\text{in}} = P_n\left\{\Psi_{\text{PM}}i_{q,\text{in}} + \left(L_{d,\text{in}} - L_{q,\text{in}}\right)i_{d,\text{in}}i_{q,\text{in}} + M_{d,\text{in}}i_{d,\text{out}}i_{q,\text{in}} - M_{q,\text{in}}i_{q,\text{out}}i_{d,\text{in}}\right\} \tag{4}$$

TABLE II
DESIGN VARIABLES IN INITIAL DESIGN

	VARIABLES	Result in	Constants
Field	PM center dia., D_{PM} PM thick., t_{PM}	PM amount - rotor shape - stator area	pole angle, air gap length, rotor yoke thick.
Arm-ature	Slot/stator ratio outer, η_o Slot/stator ratio inner, η_i	Stator shape - outer slot - inner slot	tooth/yoke ratio, slot open width, tooth tip thick.

TABLE III
DESIGN CONSTRAINTS

CONSTRAINTS	UNIT	VALUE	Comment
Number of pole pairs	-	7	
Number of slots	-	12	
Slot fill factor	%	34.6	outer/inner same
Current density	A_{rms}/mm^2	30.9	
DC link voltage	V	48	
Load coefficient	Nm/rpm^2	3.134e-7	propeller

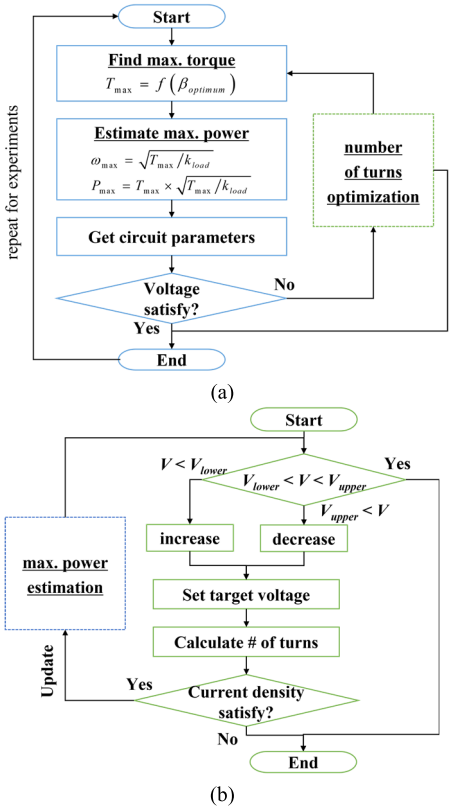

Fig. 7. Flow diagrams of initial design. (a) Maximum power estimation. (b) Number of turns optimization.

gaps and three MMF sources. Therefore, it is more critical to decide the motor shape for optimum MMF distribution. The motor shape can simply be decided with four MMF-related design variables, as shown in Table II. The numerous cases of motor shape are examined to estimate their maximum powers by fast and accurate method via FEA, as shown in Fig. 7(a). Given the motor shape, an initial value of the number of turns is set to find maximum torque, which is obtained via FEA. Because the torque is maximum when the current is maximum, the current amplitude is fixed as the maximum value, but the current phase is the variable. Under the phase angle of $\beta_{optimum}$ that is for the maximum torque, the motor circuit parameters, such as inductances and resistance, are figured out using the FEA results and dimensions. Since the maximum torque needs to be accompanied by maximum speed because of the characteristics of the propeller load, the maximum power of the model can be simply calculated. The required speed for the maximum torque is calculated by the second-order polynomial model of target propeller. At the maximum speed and torque, the voltage equation is solved with previously identified circuit parameters. If it is not satisfied, the number of turns needs to be changed, and this loop is repeated until the voltage is satisfied. To minimize the number of iterations, the relation between the number of turns and the circuit parameters is utilized as expressed in (5), as shown at the bottom of the page. These parameters are applied to the voltage equation to predict the appropriate number of turns for the desired target voltage as shown in (6), as shown at the bottom of the page, where k_R, k_L, and k_{psi} are the coefficients of resistance, inductance, and flux linkage due to PM, respectively, and these are obtained via FEA. Here, the *dq* inductances of both self and mutual between inner and outer components are expressed as merged terms for simplicity. In Fig. 7(b), V_{target} is the target voltage, which is used to calculate the new number of turns, N. ω_{base} is the base speed in rad/s at the current step. By setting the voltage target of next step, the number of turns can be obtained by solving the fourth-order equation.

B. Design Example

A commercial outer rotor SPMSM for small drones and a propeller was selected as a design target. Its maximum power is 2.0 kW, and it has 14-pole, 12-slot with tooth-concentrated winding. The design constraints are shown in Table III. Here, the load coefficient represents the coefficient of second-order polynomial of propeller model. Considering the dimensional constraints, the boundaries of the four MMF-related design variables are decided, as shown in Table IV. Total 251 cases were examined via the maximum power estimation method, and the results are shown in Fig. 8(a). Among the results, the combinations of the slot/stator ratio

$$R_a = k_R N^2, \quad L = k_L N^2, \quad \Psi_{PM} = k_{psi} N \tag{5}$$

$$V_{target} = \sqrt{\left(k_R N^2 i_d - \omega_{base} k_{Lq} N^2 i_q\right)^2 + \left(k_R N^2 i_q + \omega_{base} k_{Ld} N^2 i_d + \omega_{base} k_{psi} N\right)^2} \tag{6}$$

TABLE IV
BOUNDARIES OF DESIGN VARIABLES IN INITIAL DESIGN

VARIABLES	UNIT	BOUNDARY		
		LOWER	UPPER	STEP
PM diameter	mm	50	70	2.5
PM thickness	mm	2	5	1
Slot area ratio outer	%	40	70	10
Slot area ratio inner	%	40	70	10

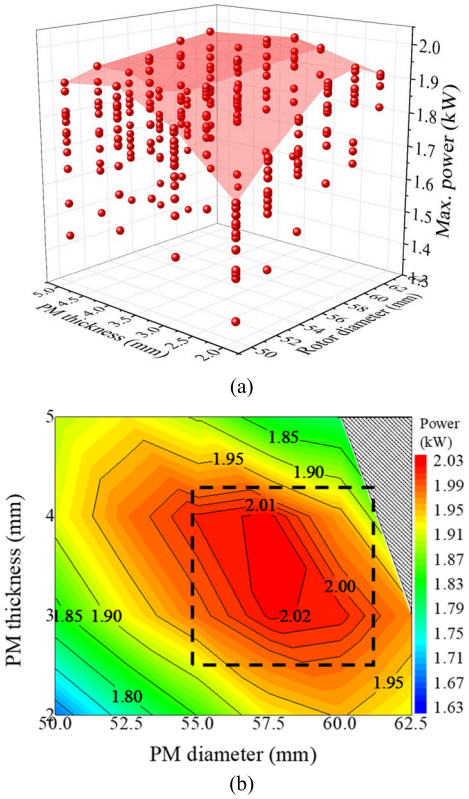

Fig. 8. Maximum power estimation results. (a) Maximum power of each case. (b) Highest maximum power according to PM shapes.

outer and inner with the highest maximum power for each PM thickness and diameter combination are shown in contour of Fig. 8(b). Further investigation was conducted to decide the pole ratio (i.e., pole angle divided by pole pitch), and three models are shown in Tables V and VI. Models with maximum power higher than the target motor were selected as candidates and SCVC was applied. Models 1 and 2 have difference in the current ratio.

C. Separated Current Vector Control

In the proposed current vector control method, SCVC, both the current amplitudes and current phase angles of the outer and inner armature are differently controlled to maximize the efficiency and minimize the torque ripple. First, the outer and inner current amplitude ratio is controlled to improve the efficiency. The total torque is proportional to the total current as expressed in the following equations:

$$I_{\text{total}} = I_{\text{outer}} + I_{\text{inner}}\ , \quad I_{\text{ratio}} = I_{\text{outer}}/I_{\text{inner}} \tag{7}$$

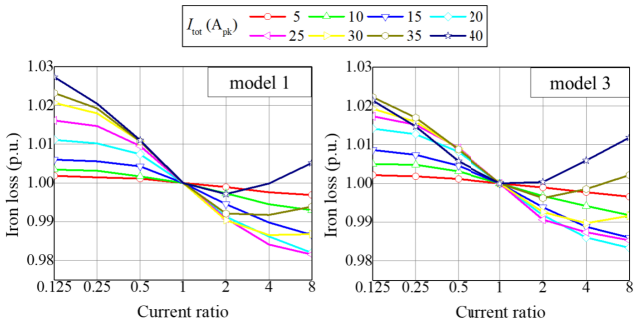

Fig. 9. Iron loss trends according to current ratio.

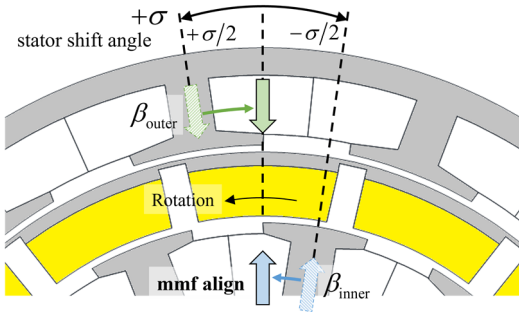

Fig. 10. Phase shift technique.

$$T_{\text{total}} = P_{\text{n}}(\phi_{\text{outer}} N_{\text{outer}} I_{\text{outer}} + \phi_{\text{inner}} N_{\text{inner}} I_{\text{inner}}) \cos\beta \tag{8}$$

$$T_{\text{total}} = P_{\text{n}} \Psi_{\text{a}} (I_{\text{outer}} + I_{\text{inner}}) \cos\beta = P_{\text{n}} \Psi_{\text{a}} I_{\text{total}} \cos\beta \tag{9}$$

where Ψ_{PM} is the armature flux linkage due to PM and ϕ_{PM} is flux due to PM. I and β are the armature current and current phase angle, respectively. The magnetic circuit of flux due to PM passes through both the outer and the inner stator and there is an only slight difference between the outer and the inner leakage flux. Since the dc-link voltage and the magnetic flux due to PM are the same on the outer and inner winding, the outer and inner numbers of turns are determined almost the same. Thus, the total torque can be expressed as (9), and it shows that the current ratio has no influence on the total torque. On the other hand, total copper loss is affected by the current ratio as shown in the following equation:

$$\begin{aligned} P_{\text{cu, total}} &= P_{\text{cu, outer}} + P_{\text{cu, inner}} = I_{\text{outer}}^2 R_{\text{outer}} + I_{\text{inner}}^2 R_{\text{inner}} \\ &= \frac{I_{\text{ratio}}^2 R_{\text{outer}} + R_{\text{inner}}}{(I_{\text{ratio}} + 1)^2} \times I_{\text{total}}^2 \end{aligned} \tag{10}$$

where P_{cu} is the copper loss. In addition, the iron loss is influenced by the current ratio as shown in Fig. 9 of the iron loss trends obtained via FEA. Consequently, the minimum loss control method to determine the current ratio needs to be applied to the proposed topology rather than the maximum torque per ampere control that is normally used in PMSM control.

Second, a phase shift as a technique of SCVC is proposed. A design variable, stator shift angle, is introduced to define the relative angular position of two stator cores, as shown in Fig. 10. This variable is determined to reduce the torque harmonics. When the stators are shifted, each armature MMF is also shifted, which results in the misalignment between the

TABLE V
POWER OPTIMIZATION—DESIGN RESULT OF THREE MODELS

Model	D_{PM} (mm)	t_{PM} (mm)	Pole ratio	Number of turns per phase		Phase resistance (Ω)		SLOT AREA (MM^2)	
				Outer	Inner	Outer	Inner	Outer	inner
1	58.0	3.4	0.875	58.9	58.3	0.134	0.063	21.0	37.9
2	56.0	3.6	0.850	64.1	64.1	0.114	0.078	29.4	33.8
3	55.0	3.7	0.850	63.2	62.3	0.103	0.084	31.5	319

TABLE VI
POWER OPTIMIZATION—CHARACTERISTICS OF THREE MODELS

Model	Power (kW)	Torque (Nm)	Speed (rpm)	Voltage (V_{rms})		Phase current (A_{rms})			Current phase (°)
				Outer	Inner	Outer	Inner	Ratio	
1	2.050	4.93	3968	31.88	31.88	15.13	27.30	1.80	7.11
2	2.026	4.90	3952	31.87	31.89	19.72	22.71	1.15	8.63
3	2.015	4.88	3945	31.87	31.89	21.08	21.35	1.01	8.12
target	2.023	4.89	3950			-			

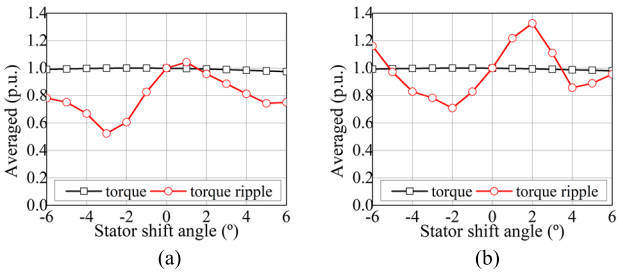

Fig. 11. Torque trends according to stator shift angle. (a) Model 1. (b) Model 3.

armature and field MMFs. To maintain the torque constant, the outer and inner current phases need to be aligned to the field MMF so that the current phase angles of the two armatures need to be controlled independently, which is possible due to the SCVC. The impact of the stator shift angle on torque characteristics is investigated, as shown in Fig. 11. Regardless of the model, the mean torque was almost constant when the stator shift angle is applied, while the torque ripple changes dramatically. Therefore, the optimum stator shift angle can be found where the torque ripple is minimum, while the mean torque is maintained. The optimum points of Models 1 and 3 are different since their torque harmonics are not equal. Since the same pole and slot number combination was applied, torque harmonics caused by cogging effect are the same so that the torque ripple trends according to the stator shift angle of two models are similar. However, their core shapes and current ratios are different, and it results in the different flux density distributions that have influence on the torque harmonics. Therefore, the optimum stator shift angles are different from each other.

IV. VERIFICATION

For the experimental verification, Model 3 was manufactured, as shown in Fig. 12(a), and the motor assembly is shown in Fig. 12(b). First, the load test was conducted with the setup

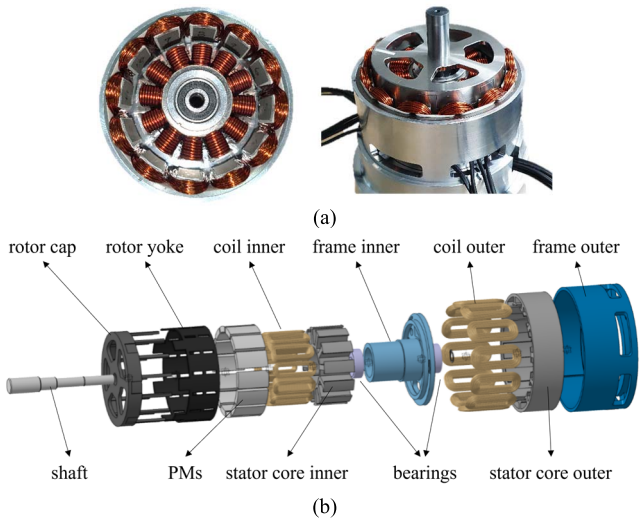

Fig. 12. Manufactured model. (a) Manufactured motor. (b) Exploded view.

shown in Fig. 13. When the outer and the inner current are the same, the torque was measured at various conditions and shown in Fig. 14. From low to high current condition, the highest torque error between the test result and FEA was 2.5%, which is an acceptable level. Next, the efficiency predicted by FEA used in this article was compared by test results, as shown in Fig. 15. To calculate the efficiency, the output power was obtained by measuring the torque and speed with torque sensor, and the input power was obtained via the power analyzer, which was wired with two of three-phase armature sets. Four comparison conditions are organized in Table VII. In this test, the same phase current was applied to both the outer and inner winding sets. The efficiency error was less than 1%p at low speed regardless of the current. Even though the error was larger at high speed, it is still acceptably small.

Second, the verification of the current ratio control was conducted. The efficiency trend according to the current ratio was measured and compared with the FEA result, as shown

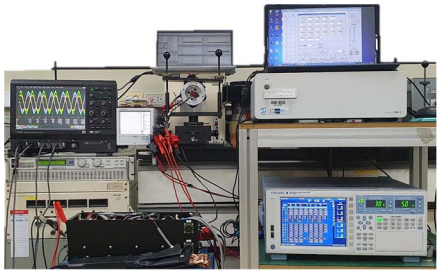

Fig. 13. Load test setup.

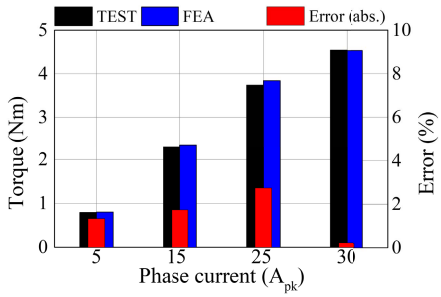

Fig. 14. Comparison of torque according to current at stall condition.

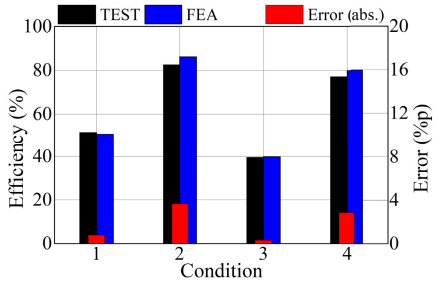

Fig. 15. Comparison of efficiency at various conditions.

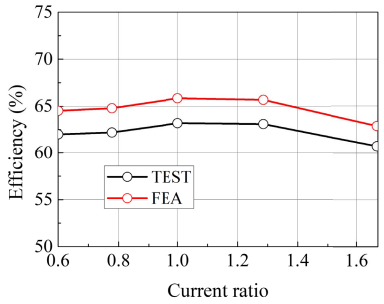

Fig. 16. Comparison of efficiency trend according to current ratio.

in Fig. 16, and test conditions are organized in Table VIII. It should be considered that the mechanical loss was ignored when calculating the FEA efficiency. Thus, the constant error at all conditions can be left out of discussion. Instead, the same trend according to the current ratio verifies the FEA result.

Finally, the phase shift technique was verified. In Fig. 17, the FEA result showed that the 12th harmonic was reduced at the stator shift angle −1° and the 6th and 12th harmonics were decreased at −5°. Therefore, the test was conducted at

TABLE VII
EFFICIENCY TEST CONDITIONS ACCORDING TO PHASE CURRENT AND SPEED

Condition	Phase current (A_{rms})	Speed (rpm)
1	16	515
2	16	3506
3	24	530
4	24	3520

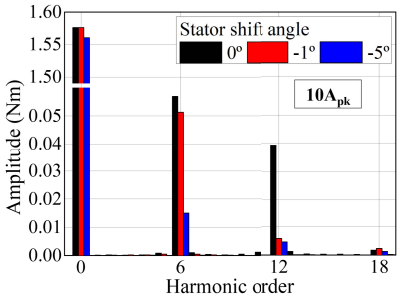

Fig. 17. FEA results of torque harmonics at different stator shift angles.

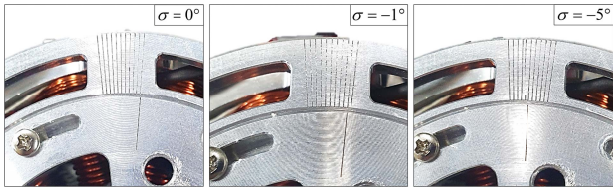

Fig. 18. Stator shift angle setup.

TABLE VIII
EFFICIENCY TEST CONDITIONS ACCORDING TO CURRENT RATIO

Condition	Phase current (A_{rms})			Speed (rpm)
	Outer	Inner	Ratio	
1	6	10	0.60	501
2	7	9	0.78	486
3	8	8	1.00	504
4	9	7	1.29	513
5	10	6	1.67	476

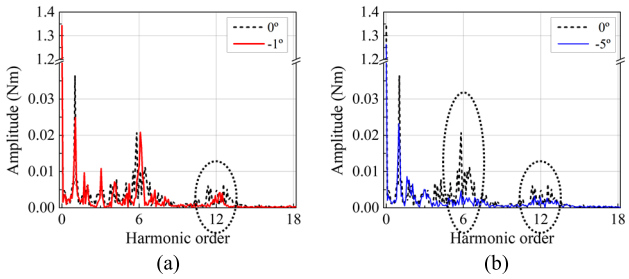

Fig. 19. Test results of torque harmonics at different stator shift angles. (a) −1°. (b) −5°.

three different stator shift angles, as shown in Fig. 18, and the results are shown in Fig. 19. The measured data exactly matched with the FEA results.

V. Conclusion

In this article, the dual stator PMSM with separately controlled dual three-phase winding was proposed. Unlike the conventional motors, the novel motor topology is advantageous to be used in eVTOL propulsion system since it can be designed and controlled to have superior quality of various requirements simultaneously. The *dq* equivalent model of the proposed topology was developed, and its inherent fault-tolerance characteristics was investigated. The design process considering the SCVC was established and its design example was presented. The unique design variables of the dual stator structures, the split ratio of the outer and inner stator cores, and the stator shift angle were designed to maximize the power density and minimize the torque ripple. In accordance with the design variables, the current ratio and current phase angles of the two armatures were determined to maximize the efficiency and torque, respectively. Finally, the experimental verification of the impact of the proposed design and control techniques was conducted. The major contributions of this article are given as follows. First, the novel motor topology was proposed for the eVTOL propulsion system. Second, the appropriate design process considering the separated control method was established to maximize the potential of the proposed motor topology. Consequently, this article is expected to facilitate the emerging trend of the electrified aircraft applications.

References

[1] P. Wheeler, T. S. Sirimanna, S. Bozhko, and K. S. Haran, "Electric/hybrid-electric aircraft propulsion systems," *Proc. IEEE*, vol. 109, no. 6, pp. 1115–1127, Jun. 2021.

[2] Y. Terao, W. Kong, H. Ohsaki, H. Oyori, and N. Morioka, "Electromagnetic design of superconducting synchronous motors for electric aircraft propulsion," *IEEE Trans. Appl. Supercond.*, vol. 28, no. 4, pp. 1–5, Jun. 2018.

[3] R. C. Bolam, Y. Vagapov, and A. Anuchin, "A review of electrical motor topologies for aircraft propulsion," in *Proc. 55th Int. Universities Power Eng. Conf. (UPEC)*, Sep. 2020, pp. 1–6.

[4] M. Ehsani, Y. Gao, and J. M. Miller, "Hybrid electric vehicles: Architecture and motor drives," *Proc. IEEE*, vol. 95, no. 4, pp. 719–728, Apr. 2007.

[5] S. A. Rizzi *et al.*, "Urban air mobility noise: Current practice, gaps, and recommendations," Langley Res. Center, NASA, Washington, DC, USA, Tech. Rep. NASA/TP-2020-5007433, 2020. [Online]. Available: https://ntrs.nasa.gov/api/citations/20205007433/downloads/NASA-TP-2020-5007433.pdf

[6] W. Cao, B. C. Mecrow, G. J. Atkinson, J. W. Bennett, and D. J. Atkinson, "Overview of electric motor technologies used for more electric aircraft (MEA)," *IEEE Trans. Ind. Electron.*, vol. 59, no. 9, pp. 3523–3531, Sep. 2012.

[7] D. Golovanov, L. Papini, D. Gerada, Z. Xu, and C. Gerada, "Multidomain optimization of high-power-density PM electrical machines for system architecture selection," *IEEE Trans. Ind. Electron.*, vol. 65, no. 7, pp. 5302–5312, Jul. 2018.

[8] K.-T. Kim, K.-S. Kim, S.-M. Hwang, T.-J. Kim, and Y.-H. Jung, "Comparison of magnetic forces for IPM and SPM motor with rotor eccentricity," *IEEE Trans. Magn.*, vol. 37, no. 5, pp. 3448–3451, Sep. 2001.

[9] G. Feng, C. Lai, W. Li, J. Tjong, and N. C. Kar, "Open-phase fault modeling and optimized fault-tolerant control of dual three-phase permanent magnet synchronous machines," *IEEE Trans. Power Electron.*, vol. 34, no. 11, pp. 11116–11127, Nov. 2019.

[10] X. Jiang, W. Huang, R. Cao, Z. Hao, and W. Jiang, "Electric drive system of dual-winding fault-tolerant permanent-magnet motor for aerospace applications," *IEEE Trans. Ind. Electron.*, vol. 62, no. 12, pp. 7322–7330, Dec. 2015.

[11] M. Barcaro, N. Bianchi, and F. Magnussen, "Analysis and tests of a dual three-phase 12-slot 10-pole permanent-magnet motor," *IEEE Trans. Ind. Appl.*, vol. 46, no. 6, pp. 2355–2362, Nov. 2010.

[12] S. Kallio, M. Andriollo, A. Tortella, and J. Karttunen, "Decoupled d-q model of double-star interior-permanent-magnet synchronous machines," *IEEE Trans. Ind. Electron.*, vol. 60, no. 6, pp. 2486–2494, Jun. 2013, doi: 10.1109/TIE.2012.2216241.

[13] Y. Hu, Z. Q. Zhu, and M. Odavic, "Comparison of two-individual current control and vector space decomposition control for dual three-phase PMSM," *IEEE Trans. Ind. Appl.*, vol. 53, no. 5, pp. 4483–4492, Oct. 2017, doi: 10.1109/TIA.2017.2703682.

[14] H. Lu, J. Li, R. Qu, D. Ye, Y. Lu, and R. Zhang, "Post-fault model predictive control of asymmetrical six-phase permanent magnet machine with improved mathematical model," in *Proc. IEEE Int. Electric Mach. Drives Conf. (IEMDC)*, May 2017, pp. 1–7, doi: 10.1109/IEMDC.2017.8002332.

[15] Y. Hu, Y. Feng, and X. Li, "Fault-tolerant hybrid current control of dual three-phase PMSM with one phase open," *IEEE J. Emerg. Sel. Topics Power Electron.*, vol. 10, no. 3, pp. 3418–3426, Jun. 2022, doi: 10.1109/JESTPE.2020.3032668.

[16] H. S. Che, M. J. Duran, E. Levi, M. Jones, W.-P. Hew, and N. A. Rahim, "Postfault operation of an asymmetrical six-phase induction machine with single and two isolated neutral points," *IEEE Trans. Power Electron.*, vol. 29, no. 10, pp. 5406–5416, Oct. 2014, doi: 10.1109/TPEL.2013.2293195.

[17] L. Wu, M. Zhu, D. Wang, and Y. Fang, "A subdomain model for open-circuit field prediction in dual-stator consequent-pole permanent magnet machines," *IEEE Trans. Magn.*, vol. 55, no. 8, pp. 1–12, Aug. 2019.

[18] Y. Zhang, S. Yu, G. Liu, and H. Zhang, "Comparative research for a novel dual-stator synchronous machine with permanent magnet-reluctance composite rotor," *IEEE Trans. Appl. Supercond.*, vol. 30, no. 4, pp. 1–5, Jun. 2020.

[19] Z. Zhang, S. Yu, F. Zhang, S. Jin, and X. Wang, "Electromagnetic and structural design of a novel low-speed high-torque motor with dual-stator and PM-reluctance rotor," *IEEE Trans. Appl. Supercond.*, vol. 30, no. 4, pp. 1–5, Jun. 2020.

[20] J. Hou, W. Geng, T. Zhu, Y. Zhang, Q. Li, and Z. Zhang, "A new hybrid excitation machine with dual-stator single-rotor axial-flux topology for electric vehicle traction application," in *Proc. 24th Int. Conf. Electr. Mach. Syst. (ICEMS)*, Oct. 2021, pp. 1342–1347, doi: 10.23919/ICEMS52562.2021.9634587.

[21] H. Yang *et al.*, "Novel dual-stator machines with biased permanent magnet excitation," *IEEE Trans. Energy Convers.*, vol. 33, no. 4, pp. 2070–2080, Dec. 2018.

[22] R. Zhu, C. Di, X. Bao, and J. Liu, "Influence of the slots number combinations among the inner and outer stator on torque ripple in dual-stator permanent magnet synchronous motors," in *Proc. 24th Int. Conf. Electr. Mach. Syst. (ICEMS)*, Oct. 2021, pp. 1137–1141, doi: 10.23919/ICEMS52562.2021.9634503.

[23] T. Zhou and L. Zhu, "The structure of symmetrical stator core offset to reduce cogging torque," in *Proc. IEEE 4th Student Conf. Electr. Mach. Syst. (SCEMS)*, Dec. 2021, pp. 1–4, doi: 10.1109/SCEMS52239.2021.9646111.

[24] Y. Zhao, W. Huang, W. Jiang, X. Lin, and X. Wu, "Optimal design and performance analysis of dual-stator permanent magnet fault-tolerant machine," *IEEE Trans. Magn.*, vol. 57, no. 2, pp. 1–6, Feb. 2021, doi: 10.1109/TMAG.2020.3026327.

[25] Y. Zhao, W. Huang, W. Jiang, X. Lin, and X. Wu, "A hybrid-slot radial-flux dual-stator permanent-magnet machine with fault-tolerant consideration," *IEEE Trans. Transport. Electrific.*, vol. 7, no. 1, pp. 214–224, Mar. 2021, doi: 10.1109/TTE.2021.3049466.

[26] R. R. Kumar, C. Chetri, P. Devi, A. Kumari, K. Kumar, and R. K. Saket, "Electromagnetic feature study of a novel dual-stator five-phase spoke-type permanent magnet motor for electric vehicles application," in *Proc. IEEE Int. Power Renew. Energy Conf. (IPRECON)*, Sep. 2021, pp. 1–6, doi: 10.1109/IPRECON52453.2021.9641005.

[27] Y. Fang, R. Ni, and T. Jiang, "Torque optimization control of dual-gap dual-pole composite machine for high efficiency and high dynamic performance," in *Proc. 24th Int. Conf. Electr. Mach. Syst. (ICEMS)*, Oct. 2021, pp. 632–635, doi: 10.23919/ICEMS52562.2021.9634600.

[28] Y. Li, D. Bobba, and B. Sarlioglu, "Design and optimization of a novel dual-rotor hybrid PM machine for traction application," *IEEE Trans. Ind. Electron.*, vol. 65, no. 2, pp. 1762–1771, Feb. 2018.

[29] F.-J. Lin, Y.-C. Hung, and M.-T. Tsai, "Fault-tolerant control for six-phase PMSM drive system via intelligent complementary sliding-mode control using TSKFNN-AMF," *IEEE Trans. Ind. Electron.*, vol. 60, no. 12, pp. 5747–5762, Dec. 2013.

[30] I. Gonzalez-Prieto, M. J. Duran, and F. J. Barrero, "Fault-tolerant control of six-phase induction motor drives with variable current injection," *IEEE Trans. Power Electron.*, vol. 32, no. 10, pp. 7894–7903, Oct. 2017.

[31] H.-J. Kim, J.-S. Jeong, M.-H. Yoon, J.-W. Moon, and J.-P. Hong, "Simple size determination of permanent-magnet synchronous machines," *IEEE Trans. Ind. Electron.*, vol. 64, no. 10, pp. 7972–7983, Oct. 2017.

Sung-Woo Hwang received the bachelor's degree in mechanical engineering and the Ph.D. degree in automotive engineering from Hanyang University, Seoul, South Korea, in 2013 and 2021, respectively.

From 2017 to 2019, he was a Research Engineer with Keyang Electric Machinery, Seoul. Since 2021, he has been with Hanyang University as a Post-Doctoral Researcher and developing digital fitness machines with electric motors as the Founder of WESPION, Seoul. His research interests include practical approaches to electric machine design for automotive and robot applications.

Dong-Kyun Son received the bachelor's degree in electrical engineering from Ulsan University, Ulsan, South Korea, in 2017. He is currently pursuing the Ph.D. degree in automotive engineering with Kookmin University, Seoul, South Korea.

His research interests include the control methods of multiphase electrical machines, sensor-less control, and nonlinear control.

Soo-Hwan Park received the bachelor's degree in mechanical engineering and the Ph.D. degree from Hanyang University, Seoul, South Korea, in 2014 and 2022, respectively.

From 2019 to 2020, he was with the Korea Institute of Industrial Technology, Daegu, South Korea. His research interests include electromagnetic field analysis, design, and optimization of electric machines for mobility system such as automotive and robotics applications, and electric machine drive for industrial applications.

Geun-Ho Lee received the B.S. and M.S. degrees in electrical engineering and the Ph.D. degree in automotive engineering from Hanyang University, Seoul, South Korea, in 1992, 1994, and 2010, respectively.

From 1994 to 2002, he was the LG Industrial Research Institute, Changwon, South Korea, where he developed an inverter system for elevators. Since 2011, he has been a Professor with the Department of Automotive Engineering, Kookmin University, Seoul, South Korea. His current research interests include advanced control of electric machines and electric vehicles.

Young-Doo Yoon (Senior Member, IEEE) was born in South Korea. He received the B.S., M.S., and Ph.D. degrees in electrical engineering from Seoul National University, Seoul, South Korea, in 2002, 2005, and 2010, respectively.

From 2010 to 2013, he was with Samsung Electronics Company, Suwon, South Korea, as a Senior Engineer. From 2013 to 2017, he was an Assistant Professor with the Department of Electrical Engineering, Myongji University, Yongin, South Korea. Since 2017, he has been an Assistant Professor with the Department of Automotive Engineering, Hanyang University, Seoul. His current research interests include power electronic control of electric machines, high-power converters, and electric home appliances.

Myung-Seop Lim (Member, IEEE) received the bachelor's degree in mechanical engineering, the master's degree in automotive engineering, and the Ph.D. degree in automotive engineering from Hanyang University, Seoul, South Korea, in 2012, 2014, and 2017, respectively.

From 2017 to 2018, he was a Research Engineer with Hyundai Mobis, Yongin, South Korea. From 2018 to 2019, he was an Assistance Professor with Yeungnam University, Daegu, South Korea. Since 2019, he has been with Hanyang University, where he is currently an Assistant Professor. His research interests include electromagnetic field analysis and multiphysics analysis of electric machinery for mechatronics systems, such as automotive and robot applications.